

2 **Micro- to nano-scale characterization of martite from a banded** 3 **iron formation in India and a lateritic soil in Brazil**

4 **Beate Orberger · Christiane Wagner · Alina Tudryn ·**
5 **Richard Wirth · Rachael Morgan · José D. Fabris ·**
6 **Jean Marc Greneche · Carlos Rosière**

7 Received: 7 October 2013 / Accepted: 9 April 2014
8 © Springer-Verlag Berlin Heidelberg 2014

9 **Abstract** The pseudomorphic transformation of magnetite into hematite (martitization) is widespread in geological environments, but the process and mechanism of this transformation is still not fully understood. Micro- and nano-scale techniques—scanning electron microscopy, focused ion beam transmission electron microscopy, and Raman spectroscopy—were used in combination with X-ray diffraction, Curie balance and magnetic hysteresis analyses, as well as Mössbauer spectroscopy on martite samples from a banded iron formation (2.9 Ga, Dharwar Craton, India), and from lateritic soils, which have developed on

siliciclastic and volcanic rocks previously affected by metamorphic fluids (Minas Gerais, Brazil). Octahedral crystals from both samples are composed of hematite with minor patches of magnetite, but show different structures. The Indian crystals show trellis of subhedral magnetite hosting maghemite in sharp contact with interstitial hematite crystals, which suggests exsolution along parting planes. Grain boundary migrations within the hematite point to dynamic crystallization during deformation. Dislocations and fluid inclusions in hematite reflect its precipitation related to a hydrothermal event. In the Brazilian martite, dislocations are observed and maghemite occurs as Insel structures and nano-twin sets. The latter, typical for the hematite, are a transformation product from maghemite into hematite. For both samples, a deformation-induced hydrothermally driven transformation from magnetite via maghemite to hematite is proposed. The transformation from magnetite into maghemite comprises intermediate non-stoichiometric magnetite steps related to a redox process. This study shows that martite found in supergene environment may result from earlier hypogene processes.

A1 B. Orberger (✉)
A2 ERAMET RESEARCH, 1 Avenue Albert Einstein,
A3 78190 Trappes, France
A4 e-mail: beate.orberger1@orange.fr

A5 B. Orberger · A. Tudryn · R. Morgan
A6 Université Paris-Sud, Laboratoire GEOPS,
A7 UMR 8148 (CNRS-UPS), Bât 504, 91405 Orsay, France

A8 C. Wagner
A9 UPMC, Univ Paris 06, IStEP, CNRS, UMR 7193, 4 Place
A10 Jussieu, 75005 Paris, France

A11 R. Wirth
A12 Department 4, GeoForschungsZentrum Potsdam (GFZ),
A13 Telegrafenberg, 14482 Potsdam, Germany

A14 J. D. Fabris
A15 Universidade Federal dos Vales do Jequitinhonha e Mucuri,
A16 Diamantina, Minas Gerais 39100-00, Brazil

A17 J. M. Greneche
A18 LUNAM, Institut des Molécules et Matériaux du Mans, IMMM
A19 UMR CNRS 6283, Université du Maine, 72085 Le Mans, France

A20 C. Rosière
A21 Instituto de Geociências, Universidade Federal de Minas Gerais,
A22 Belo Horizonte, Minas Gerais 31270-901, Brazil

Keywords Magnetite · Hematite · Maghemite ·
FIB-TEM · Raman · Mössbauer

Introduction

In nature, magnetite is transformed into hematite often via pseudomorphic replacement, which was first described by Gruner (1922, 1926, 1929). The chemical and crystallographic transformation of magnetite (FeOFe_2O_3 , cubic crystallographic structure) into hematite ($\alpha\text{-Fe}_2\text{O}_3$, trigonal) perfectly preserves the octahedral crystal habit of the magnetite precursor. This replacement (or martitization)

51 leads to the formation of so-called “martite”. In the text,
 52 the word “martitization and martite” will thus be used as
 53 defined above and as used by, e.g., Swanson-Hysell et al.
 54 (2011) and papers therein. The magnetite replacement by
 55 hematite can occur during oxidation via O^{2-} addition or
 56 Fe^{2+} loss (Lepp 1957; Davis et al. 1968). Alternatively, a
 57 dissolution–precipitation process (chemically or biochemi-
 58 cally mediated) can be controlled by pH changes (Brown
 59 et al. 1997; Ohmoto 2003; Otake et al. 2007) or by defor-
 60 mation (Lagoeiro 1998). All these processes have been
 61 proposed for banded iron formations (BIFs), where the
 62 magnetite–hematite transformation is common (Banerji
 63 1984; Morris 1985; Ohmoto 2003; Mücke and Cabral
 64 2005; Beukes et al. 2008). The transformation can occur
 65 directly from magnetite to hematite, as mainly observed in
 66 low-temperature sedimentary environments, or via maghemite
 67 formation ($\gamma\text{-Fe}_2\text{O}_3$, cubic with a tetragonal super-
 68 cell) as an intermediate step (Bachmann 1954; Lepp 1957;
 69 Colombo et al. 1965; Davis et al. 1968; Morris 1980, 1985;
 70 Banerji 1984). The metastability of maghemite compared
 71 to hematite has been much debated (see the review of Lind-
 72 sley 1976 and references therein). Maghemite has an iron-
 73 deficient spinel structure with vacancies distributed among
 74 the octahedral and tetrahedral sites (e.g., “kenotetrahedral
 75 magnetite” from Kullerud et al. 1969; Weber and Hafner
 76 1971). According to Lindsley (op. cit.), these spinels are
 77 considered either as “omission solid solution between mag-
 78 netite and γ - (or α -) Fe_2O_3 ” or simply as “cation—deficient

magnetites”. We use hereafter the term of “non-stoichio-
 metric magnetite” for these intermediate products.

This is the first study on martite using micro- and nano-
 scale methods, scanning electron microscopy (SEM),
 focused ion beam transmission electron microscopy (FIB-
 TEM) and micro-Raman spectroscopy, which were crossed
 with X-ray diffraction (XRD), Mössbauer spectroscopy,
 Curie balance and magnetic hysteresis in order to under-
 stand the processes and mechanisms of the magnetite–hem-
 atite transformation. We studied two samples from different
 geological environments. The first belongs to chemically
 precipitated BIFs, which were affected by lower green-
 schist facies metamorphism (Bababudan Group; 2.9 Ga,
 Mid-Archean Western Dharwar Craton, Southern India;
 Orberger et al. 2012). The second sample comes from a
 lateritic soil, which developed on siliciclastic and volcanic
 rocks previously affected by metamorphic fluids (Mid-
 Proterozoic Espinhaço Supergroup, Minas Gerais, Brazil;
 Cabral et al. 2011, 2012 and references therein).

Sample description

The Brazilian sample consists of millimetric octahedral
 crystals from a lateritic soil developed on phyllites of the
 Espinhaço Supergroup (Serra do Espinhaço, Minas Ger-
 aís, Brazil, south of the Guinda, southeast of Diamantina
 (18°17'31.12"S, 43°38'09.75"W; Fig. 1a). These rocks

Fig. 1 Brazilian sample from the Espinhaço Range, Minas Gerais. **a** Octahedral crystals. Reflected light microphotographs, polished thin section. **b** Hematite of platy structure. **c** Hematite (white) replacing magnetite (gray). *mag* magnetite, *hm* hematite

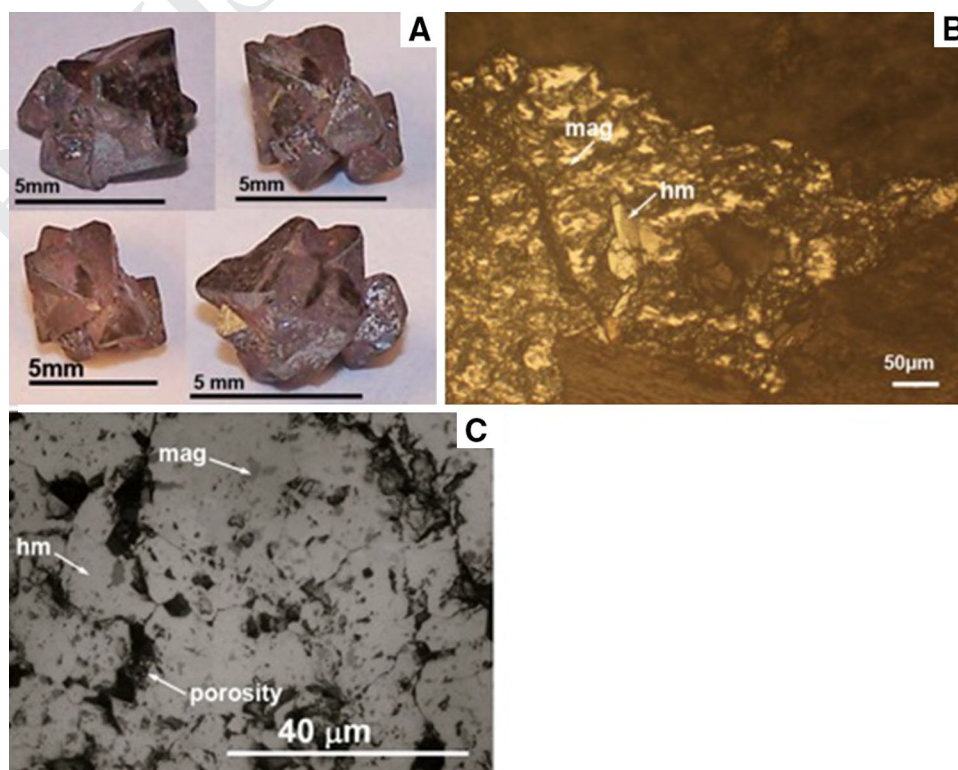
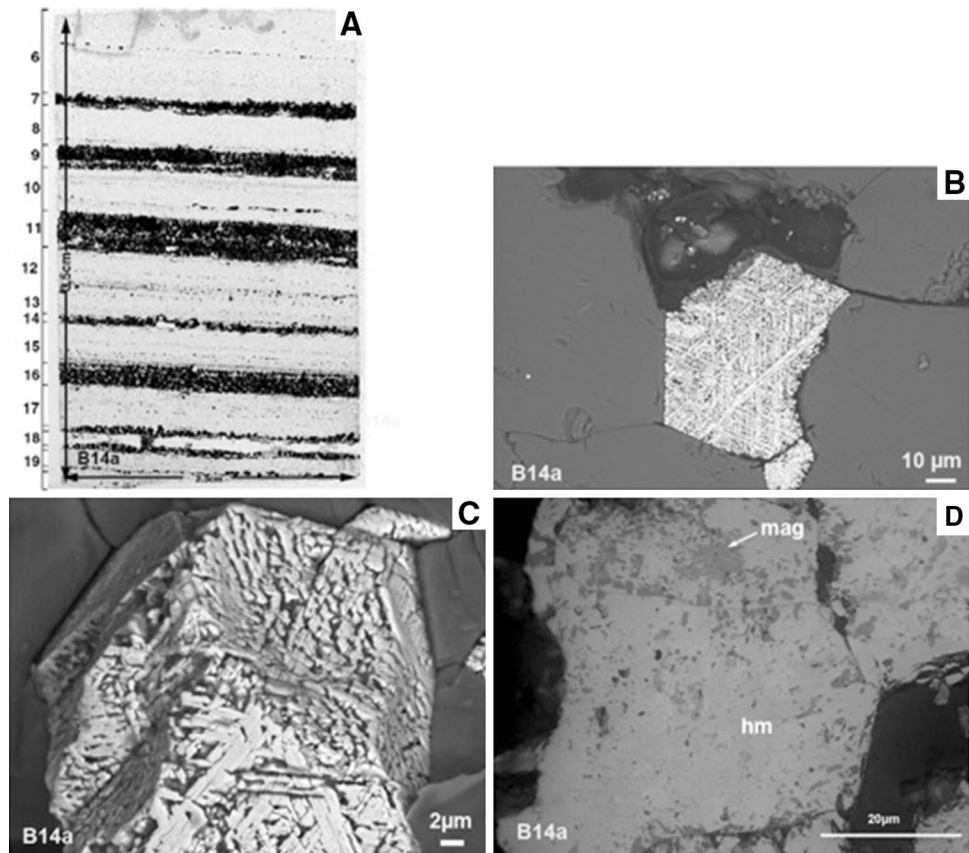


Fig. 2 **a** Scanned polished thin section of the Indian sample (B14a) from the Dharwar Craton showing alternating iron oxide (*dark*) and quartz bands (*bright*). **b** and **c** SEM–BSE microphotographs of a subhedral iron oxide crystal showing a trellis, intergrown with quartz. **d** Reflected light microphotograph of iron oxide crystals. Hematite (*white*) is the major phase with relicts patches of magnetite (*gray*) and rare goethite (*darker gray*). Symbols as in Fig. 1



104 contain magnetite, hematite and tourmaline and host hydro-
 105 thermal quartz veins with irregular aggregates of magnetite
 106 and tourmaline randomly distributed over the metamorphic
 107 fabric (Cabral et al. 2011, 2012).

108 The micro-texture of the Brazilian sample shows sub-
 109 to euhedral hematite octahedral grains (20–40 μm) show-
 110 ing intergranular porosity (Fig. 1b, c). On the outer crystal
 111 faces, carbonaceous matter was observed. Some platy hema-
 112 tite crystals (~20 μm) occur in linear clusters along crystal
 113 planes (Fig. 1b). Magnetite relicts are still present (Fig. 1c).

114 The Indian sample (B14a) comes from the 500-m-thick
 115 Archean BIF of the Bababudan Group in the Western Dhar-
 116 war Craton, Southern India (N 13°19'539", E 76°42'300"),
 117 herein referred to as the Indian sample. The BIF chemically
 118 precipitated from a mixture of hydrothermal and seawater
 119 fluids (Kumar and Das Sharma 1998; Srinivasan and Oja-
 120 kangas 1986; Orberger et al. 2012) and experienced green-
 121 schist facies metamorphism (Taylor et al. 1984; Jayananda
 122 et al. 2006; Sarma et al. 2011). The Indian sample is char-
 123 acterized by alternating millimetric layers of gray Fe-oxide
 124 and white quartz (Fig. 2a). The Fe-oxide layers consist of
 125 cubic or octahedral crystals (~20 μm) of hematite, showing
 126 a trellis pattern (Fig. 2b, c) with relicts of magnetite and
 127 rare goethite patches (Fig. 2d). Modern weathering led to
 128 the formation of goethite (Orberger et al. 2012).

Methods

129 Polished thin sections of both Brazilian and Indian samples
 130 were studied using reflected and transmitted light optical
 131 microscopy, SEM and TEM and micro-Raman spectroscopy.
 132 XRD, Curie balance, magnetic hysteresis and Möss-
 133 bauer spectrometry were performed on powders of a few
 134 macroscopic octahedra from the Brazilian sample and three
 135 separate fractions (total sample material, magnetic fraction
 136 and rest) of a massive Fe-oxide band from the Indian BIF.
 137

SEM and TEM

138 Backscattered electron (BSE) imaging was performed
 139 using SEM Philips XL 30 connected to an EDX-PGT Ge
 140 detector for semi-quantitative chemical analyses (20–
 141 30 kV) at the Université de Paris Sud XI and SEM Zeiss
 142 SUPRA 55VP at the Université Paris 06 (UPMC), Paris.
 143 Focused ion beam (FIB) technique was used to cut slices
 144 with dimensions of 10 × 10 × 0.1 μm³ for TEM. Details of
 145 the FIB milling process were given in Wirth (2004, 2009).
 146 TEM was performed using a FEI F20 X-Twin microscope
 147 with a Schottky field emitter as an electron source at GFZ-
 148 Potsdam, Germany. The TEM mode was used to assess the
 149 bright and dark field imaging and selected area electron
 150



- 151 diffraction (SAED). A Fishione high-angle annular dark
152 field (HAADF) detector enables Z-contrast imaging. The
153 chemical composition of selected spots was determined
154 with an EDAX X-ray analyzer with ultra-thin window and
155 a Li-doped silicon detector.
- 156 **Micro-Raman spectroscopy**
- 157 Raman spectroscopy was performed at the Laboratoire
158 de Sciences de la Terre, ENS-Lyon, Lyon, France, using
159 a Horiba Jobin-Yvon Labram HR800 spectrometer,
160 equipped with a microscope for the backscattered Raman
161 signal collection. Oxide phases were characterized through
162 unpolarized Raman spectra within 30–60 s. The excita-
163 tion source was an argon ion laser beam at $\lambda = 514.5$ nm.
164 The lateral resolution of the focused laser probe was meas-
165 ured at 1 mm using 100 \times objective magnification. The laser
166 power measured at the sample was 500 μ W. Calibration
167 was performed during measurements in a silicon semi-
168 conductor mode at 520.7 cm^{-1} . The spectral signals were
169 recorded in the range between 150 and 1,800 cm^{-1} . The
170 spectral resolution was $\sim 2\text{--}4$ cm^{-1} (with diffraction grating
171 of 600 gr mm^{-1} for the Indian sample and 1,800 gr mm^{-1}
172 for the Brazilian sample). The Raman spectra were pro-
173 cessed by the PeakFit 4.0 (Jandel Scientific) software using
174 Loess smoothing procedure and second-order polynomial
175 function for baseline fitting. The peak wave numbers were
176 determined assuming a Lorentzian line shape.
- 177 Laser-induced thermal effects are known to affect iron
178 oxides and hydroxides, but sample degradation can be
179 avoided using a laser power on the sample below 1 mW (She-
180 banova and Lazor 2003a; Gehring et al. 2009; El Mendili
181 et al. 2010). Thus, a low 500- μ W power was used here, and
182 moreover, we check for any possible degradation by acquir-
183 ing several spectra at the same location for a total time of
184 8 min on a goethite patch in the Indian sample as shown in
185 “Appendix”. Apart from the expected lowering of the back-
186 ground fluorescence with increasing acquisition time, no sig-
187 nificant changes in position, shape, or width of the goethite
188 characteristic peaks are noticeable. This rules out any laser-
189 induced goethite dehydration and transformation to hematite.
- 190 **XRD analyses**
- 191 XRD analyses were performed at the UMR IDES, Uni-
192 versité Paris Sud XI, using a Philips apparatus with Cu-
193 α cathode during a 4-h run between 6 $^\circ$ and 80 $^\circ$ (2θ). For
194 the Brazilian sample, two more 3-h runs were performed
195 in the ranges 34 $^\circ$ –40 $^\circ$ and 51 $^\circ$ –67 $^\circ$ in order to distinguish
196 between overlapping peaks of magnetite, maghemite and
197 hematite (Fig. 3c, d). Calibration of the XRD spectra was
198 performed with quartz, which is finely intergrown with the
199 Fe-oxides in the Indian sample. The precision is 0.004 \AA .
- Magnetic parameter analyses 200
- The thermomagnetic behavior of the samples was deter- 201
mined on a horizontal force translation balance at UMR 202
IDES, Université Paris Sud XI. Analyses were performed 203
in air atmosphere, in a magnetic field of 0.375 T and lin- 204
ear temperature increase of 10 $^\circ\text{C min}^{-1}$. Magnetic hyster- 205
esis measurements were taken at room temperature with an 206
alternating gradient magnetometer (AGM 2900-Micromag) 207
at the LSCE-CNRS/CEA laboratory at Gif-sur-Yvette, 208
France. A peak-applied field of 1 T was used for hystere- 209
sis measurements. The values of saturation magnetization 210
(M_s), saturation remnant magnetization (M_{rs}) and coercive 211
force (B_c) were estimated from the hysteresis loop; M_s and 212
 M_{rs} were mass normalized. Coercivity of remanence (B_{cr}) 213
was obtained by step-wise application of back fields to 214
remove the saturation remanence. The magnetic hysteresis 215
parameters are given in Table 1. 216
- ⁵⁷Fe-Mössbauer spectrometry 217
- ⁵⁷Fe-Mössbauer spectrometry was carried out at the Institut 218
des Molécules et Matériaux du Mans, Université du Maine, 219
Le Mans, France. Spectra were recorded in transmission 220
geometry at 300 K using a ⁵⁷Co/Rh γ -ray source mounted 221
on a conventional constant acceleration electromagnetic 222
drive. The hyperfine structure was analyzed by means of 223
a least squares fitting method involving magnetic compo- 224
nents with Lorentzian lines. The fitting procedure allows 225
estimating the hyperfine parameters of each Fe species on 226
their respective atomic proportions. The isomer shift values 227
(δ) are referred to α -Fe at 300 K (Table 2). 228
- Results** 229
- X-ray diffraction 230
- A careful study of the diffraction patterns is needed in order 231
to discriminate between the different Fe-oxides due to peak 232
overlapping of, for example, the major peaks ($I = 100$) of 233
magnetite (2.532 \AA , JCPDS 19-629; Joint Committee on 234
Powder Diffraction Standard 1974), maghemite (2.52 \AA , 235
JCPDS 4-755) and hematite ($I = 50$; 2.52 \AA), or the peak at 236
1.48 \AA ($I = 40\text{--}50$) present in these three Fe-oxides. 237
- Brazilian sample* 238
- A well-crystallized hematite with strong and sharp reflec- 239
tion peaks is the major compound (Fig. 3a). The presence 240
of maghemite is revealed by the peak at 2.782 \AA [$I = 19$ 241
(221); Fig. 3b], while the shoulder at 2.532 \AA on the major 242
hematite peak [2.518 \AA (311); Fig. 3d] could be attributed 243

Fig. 3 XRD patterns of the Brazilian sample. **a** Total spectrum, 4-h run, range 6°–80° (2θ). **b** Zoom, 26°–35° (2θ). **c** and **d** 3-h spectrum for the key areas 51°–67° (2θ) and 34°–40° (2θ), respectively. *He* hematite, *Mg* magnetite, *Mh* maghemite, *Qz* quartz, *G* goethite

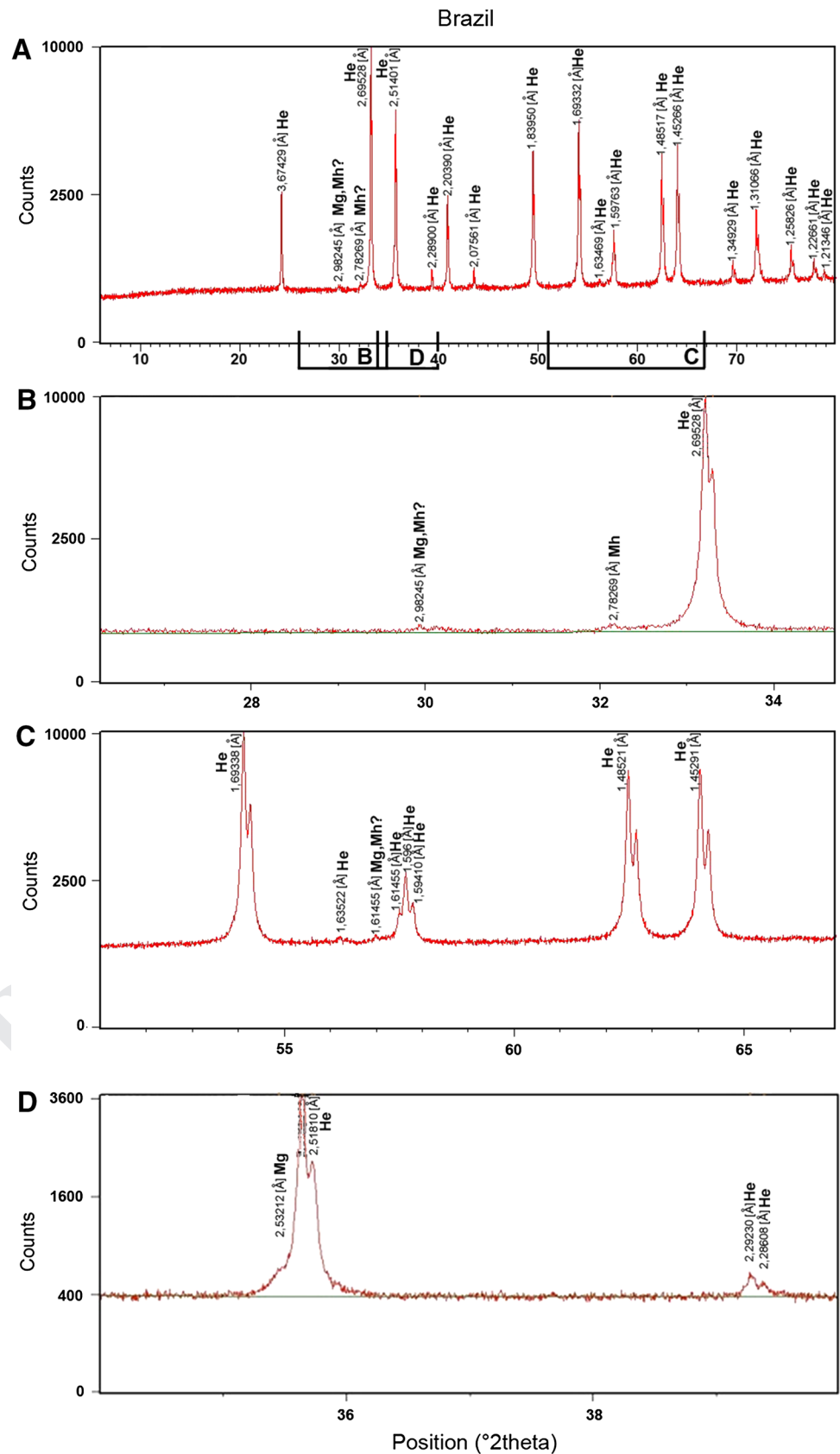


Table 1 Magnetic hysteresis parameters

Samples	B_c (mT)	B_{cr} (mT)	M_{rs}/masse ($\mu\text{Am}^2/\text{mg}$)	M_s/masse ($\mu\text{Am}^2/\text{mg}$)	M_{rs}/M_s	B_{cr}/B_c
Brazil	19.7	221.5	0.27	0.86	0.31	11.24
India total	18.8	62.4	0.28	1.62	0.17	3.32
India extract	12.9	46	0.58	4.67	0.12	3.57
India rest	21.5	78.3	0.22	1.12	0.20	3.64

B_c coercive force, B_{cr} coercivity of remanence, M_{rs} remanent magnetization, M_s saturation magnetization

Table 2 Mössbauer spectral parameters at 300 K

Values of Mössbauer parameters at 300 K					
Sample label	δ (mm/s)	2ϵ (mm/s)	B_{hf} (T)	Proportions	Oxide
	± 0.01	± 0.01	± 0.5	± 2 (%)	
India total	0.38	-0.17	51.5	86	Ht
	0.35	-0.27	37.8	14	Goeth
India MF	0.63	0 ^a	46.0	2	Mt, Fe ³⁺
	0.32	0 ^a	49.0 ^a	1	Mt, Fe ^{2.5+}
India REST	0.38	-0.17	51.5	83	Ht
	0.37	-0.26	38.0	14	Goeth
Brazil	0.38	-0.17	51.9	82	Ht
	0.36	-0.26	37.8	18	Goeth

Three separate fractions were analyzed for the Indian sample: total, magnetic fraction (MF), and rest after magnetic extraction (REST). The two components of magnetite were assumed in the expected ratio in the fitting procedure, while their respective hyperfine field (B_{hf}), quadrupolar (2ϵ), and isomer (δ) shift values were fixed to expected values, because of the lack of resolution. The magnetite components were introduced through fitting the Mössbauer spectra of the Total and REST fractions, but the final content was very low (<5 %)

Ht: hematite; Mt, Fe³⁺ and Mt, Fe^{2.5+} refer to the magnetite sextets; Goeth: goethite

^a Fixed parameter during fitting

to magnetite. Magnetite and/or maghemite may be indexed from the peak at 2.982 Å (Fig. 3b), which could correspond to the peaks 2.96 and 2.95 Å [$I = 30$ (220)] of magnetite and maghemite, respectively, and from the peak at 1.614 Å (Fig. 3c), corresponding to the peak at 1.616 Å ($I = 30/33$, 511 or 333) of the two oxides.

Indian sample

The XRD spectrum of the total sample—prior to magnetic separation—shows the presence of quartz (JCPDS 5-615), hematite and goethite (JCPDS 17-536) (Fig. 4a). Hematite is the major compound showing strong and sharp reflections, while the goethite peaks are asymmetric and show a large half-peak width, which is indicative for poor crystallinity (Fig. 4b, c). A very small peak appears at 2.787 Å, characteristic for maghemite, and at

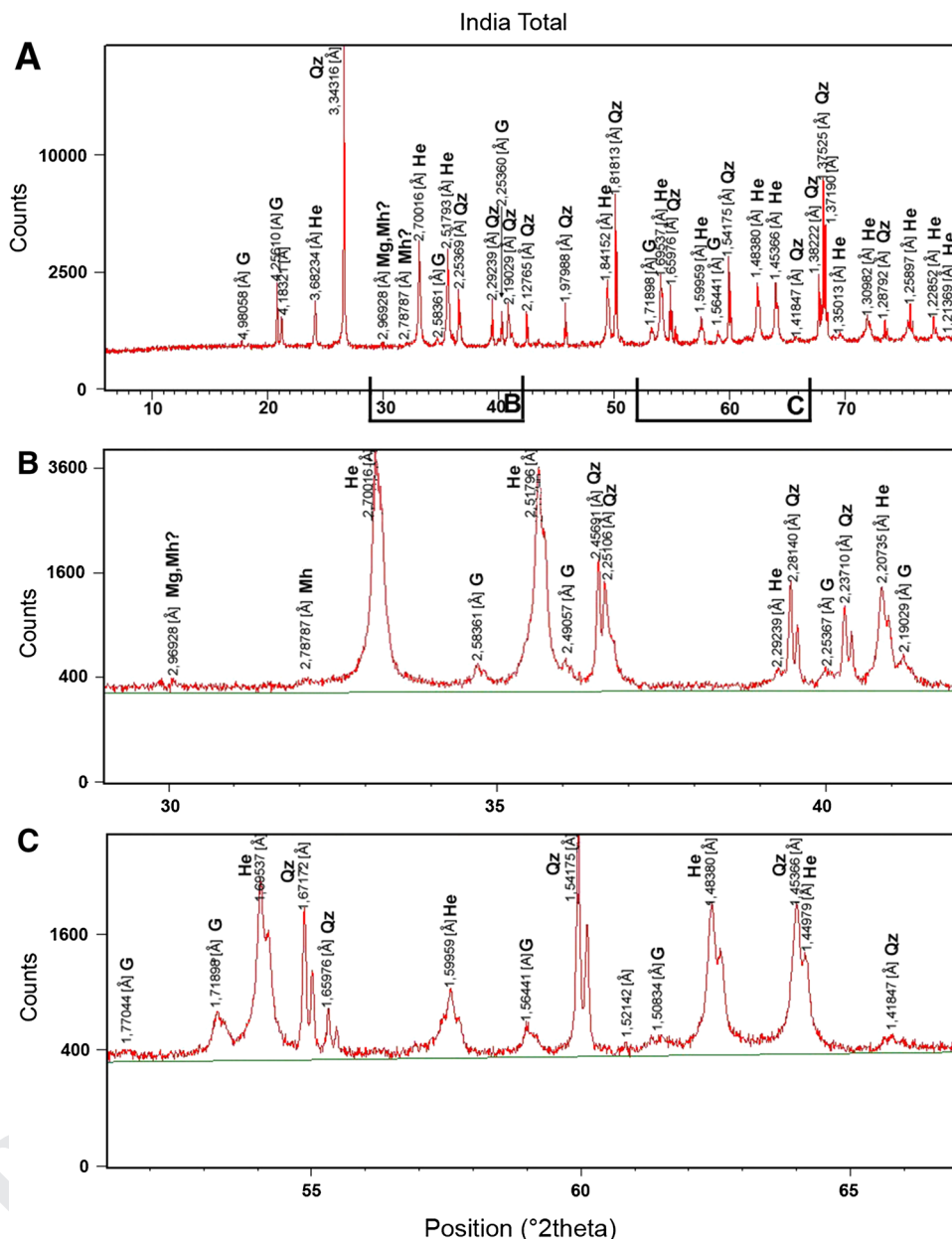
2.969 Å for possibly magnetite or maghemite (Fig. 4b). In the magnetic fraction, the same minerals as in the total sample are observed, but oxide peaks show higher intensities (Fig. 5a, c). The weak peak at 1.613 Å (Fig. 5c) may indicate magnetite or maghemite. The peak at ~2.5 Å (Fig. 5b) is split, suggesting the presence of magnetite (311) and hematite (110) or maghemite (311). The rest of the material—after magnetic separation—shows, as expected, higher intensities of quartz, no peak splitting at 2.5 Å, but still a weak peak at 2.973 Å (Fig. 6b) attributed to magnetite or maghemite.

Magnetic parameters

Both samples show a mixture of magnetite and hematite, with Curie temperatures of 580 and 680 °C, respectively (Fig. 7a, b, d). In this range of temperatures, the higher intensity of the relative magnetization (M/M_s) in the Brazilian sample compared to the Indian total fraction (Fig. 7a, b) suggests a higher content of hematite relative to magnetite in the former. In the Indian magnetic fraction (Fig. 7c), low M/M_s reflects the dominance of magnetite, a soft ferromagnetic magnetite easily magnetized and extracted from the total sample compared to hard weak magnetic hematite (canted antiferromagnetic), while hematite controls higher M/M_s in the Indian rest after magnetic extraction (Fig. 7d). The decrease in relative magnetization just below 400 °C (Fig. 7a) in the Brazilian sample, as well as the very slight decrease in the Indian rest fraction (Fig. 7d), indicates that another magnetic phase is present such as maghemite, which commonly transforms into hematite at that temperature (e.g., Tarling 1983; Thompson and Oldfield 1986; De Boer and Dekkers 2001).

Magnetic hysteresis loops are presented in Fig. 7e, h and hysteresis characterizing parameters in Table 1. The magnetic hysteresis loops of the Brazilian sample and the Indian total and rest fractions (Fig. 7e, f, h) are constricted in the middle section, and wider above and below the middle section. Such “wasp-waisted” hysteresis loops indicate different magnetic components with contrasting coercive fields and may correspond to (1) a mixture of different grain sizes of a single magnetic mineral, (2) a mixture of different magnetic materials with largely

Fig. 4 XRD patterns of the total Indian. **a** Total spectrum, 4-h run, range 6°–80° (2θ). **b** Zoom, range 29°–42° (2θ). **c** Zoom, range 51°–67° (2θ). Same symbols as in Fig. 3



300 different coercivities, or (3) a combination of both possi- 314
 301 bilities (e.g., Wasilewski 1973; Day et al. 1977; Roberts 315
 302 et al. 1995; Tauxe et al. 1996). When different magnetic 316
 303 components are present, the soft (low coercivity) compo- 317
 304 nent controls the coercive force (B_c), while the hard (high 318
 305 coercivity) component controls the coercivity of remanence 319
 306 (B_{cr}). The degree of the constriction in the middle section 320
 307 of the magnetic loop depends on the relative contribution 321
 308 of each component. Furthermore, in the presence of high 322
 309 magnetic moment minerals, such as ferrimagnetic magnet-
 310 ite or maghemite, canted anti-ferromagnetic hematite with
 311 weak magnetic moments must be abundant to cause wasp-
 312 waisted magnetic loops. The wasp-waisted hysteresis loops
 313 for the studied samples (Fig. 7e, f, h) result from a mixture

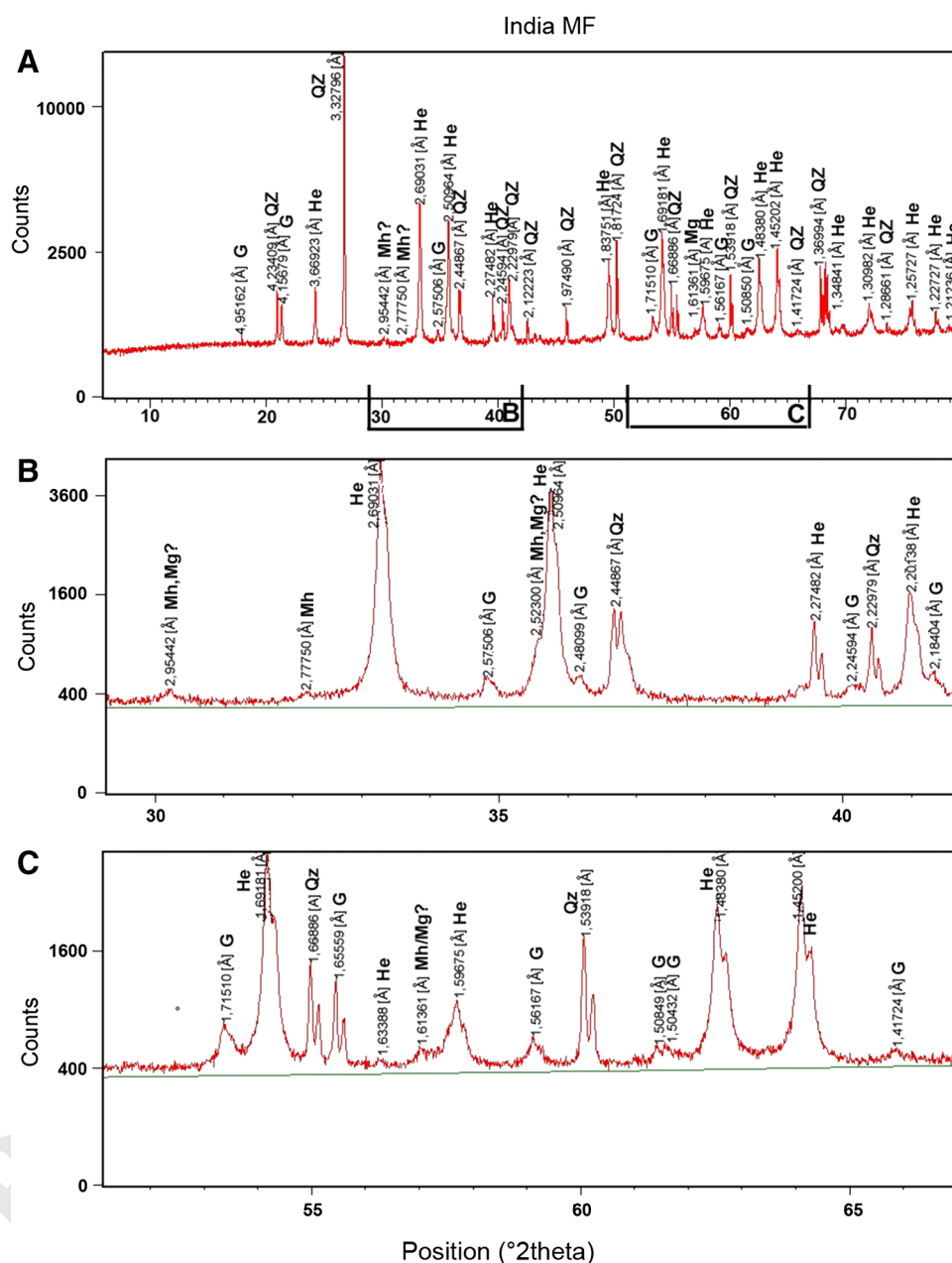
of different components. In the Brazilian sample, high B_{cr} 314
 (Table 1) and the open nature of the loop at magnetic field 315
 values above 0.3 T (corresponding to the maximum coer- 316
 civity of most ferrimagnetic minerals such as magnetite) 317
 indicate a relatively higher amount of the hard component 318
 hematite (\pm goethite) compared to magnetite (\pm maghe- 319
 mite) than in the Indian sample (Fig. 7e, f, h). In the Indian 320
 sample, low values of B_c (Table 1) indicate the presence of 321
 a soft material such as magnetite or maghemite. 322

^{57}Fe -Mössbauer spectrometry 323

The 300-K Mössbauer data of the Indian sample (total, 324
 magnetic fraction and rest after magnetic extraction) 325



Fig. 5 XRD patterns of the magnetic fraction (MF) of the Indian sample. **a** Total spectrum, 4-h run, range 6° – 80° (2θ). **b** Zoom, range 29° – 42° (2θ). **c** Zoom, range 51° – 67° (2θ). Same symbols as in Fig. 3



326 and the Brazilian sample are shown in Table 2, and pat- 327
328 terns are shown in Fig. 8. The spectrum for the Brazilian 329
330 sample consists of a single sextet evidencing the 331
332 sole occurrence of hematite. Differently, in all spectra 333
334 for the Indian sample, the hyperfine structure exhibits 335
336 spectral features that correspond to the two coordina- 337
338 tion symmetries of iron in magnetite: Fe^{3+} on tetrahedral 339
340 and $\text{Fe}^{3+/2+}$ on octahedral sites of the spinel structure. 341
342 Furthermore, in the spectrum for the magnetic fraction 343
344 of the Indian sample, the inset of Fig. 8 magnifies the— 345
346 though small—resonance line assignable to iron on octa- 347
348 hedral sites of magnetite. Both the total Indian sample 349
350 and the rest fraction after magnetic extraction indicate 351

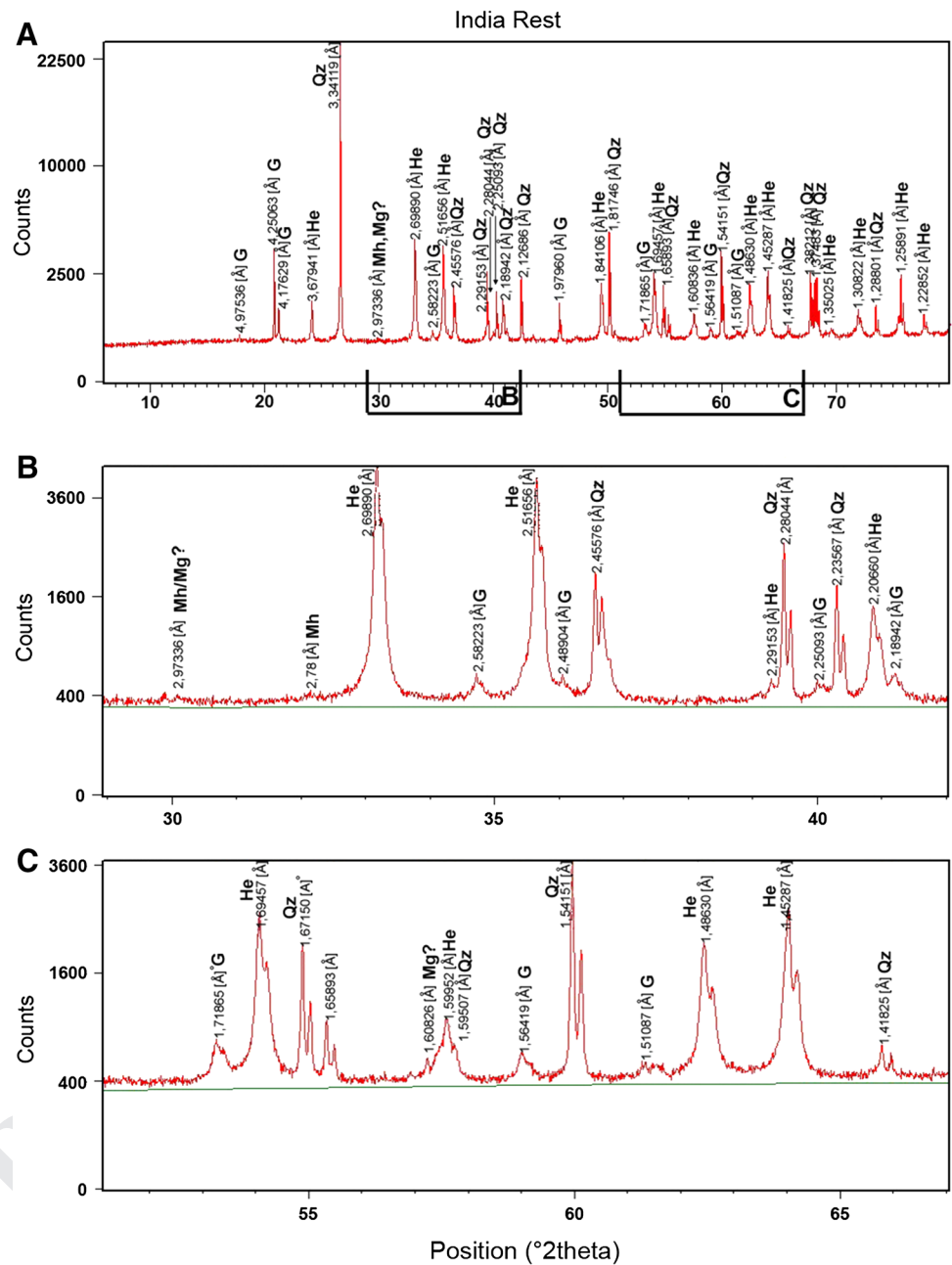
326 the presence of hematite (86 and 82 %, respectively) 327
328 and goethite (14 and 18 %, respectively), while only 329
330 3 % of magnetic fraction is composed of magnetite and 331
332 still 83 % represents the hematite. No maghemite was 333
334 detected in both samples. 335

Micro-Raman spectroscopy 344

Brazilian sample 345

346 Ten to twenty spectra were collected on selected zones of 347
348 both samples. Representative Raman spectra are shown in 349
350 Figs. 9 (Brazil) and 10 (India). 351

Fig. 6 XRD patterns of the Indian sample, rest material after magnetic separation. **a** Total spectrum, 4-h run, range 6° – 80° (2θ). **b** Zoom, range 29° – 42° (2θ). **c** Zoom, range 51° – 67° (2θ). Same symbols as in Fig. 3



349 In the Brazilian sample, spectra were recorded from
 350 two different grains based on differences in reflected light:
 351 (1) rare small (5–20 μm) dark grayish patches in (2) over-
 352 all bright white grains. In the bright areas, the spectra
 353 recorded from grain 1 (Fig. 9a) show bands at 222–229,
 354 293–304, 413–419, 505–512, 614–633, 664–679, and
 355 1,336–1,342 cm^{-1} , while in grain 2 (spectrum not shown),
 356 an additional band at 248–250 cm^{-1} appears. The band
 357 at $\sim 300 \text{ cm}^{-1}$ may be split into two bands (e.g., 291 and
 358 299 cm^{-1}). This combination of bands is typical of hem-
 359 atite (e.g., de Faria et al. 1997; Hanesh 2009). Hematite
 360 belongs to the D_{3d}^6 spatial group, and seven Raman active

361 modes are expected: two A_{1g} modes at 225 and 498 cm^{-1}
 362 and five E_g modes at 247, 293, 299, 412, and 613 cm^{-1} ,
 363 and a band at 1,320 cm^{-1} usually attributed to a two-mag-
 364 non scattering (de Faria et al. 1997). Some bands may not
 365 be resolved or may only appear on the flank of stronger
 366 peaks (e.g., bands at 245 and 299 cm^{-1}) as observed here
 367 (op. cit.). In our samples, the peak positions are slightly
 368 shifted toward greater wave numbers compared to the
 369 aforementioned data. This may be due to different laser
 370 wavelengths and powers, the crystallinity or the orienta-
 371 tion of the sample, and is meaningless. However, the addi-
 372 tional band at 668–675 cm^{-1} , the position of the E_{g5} mode

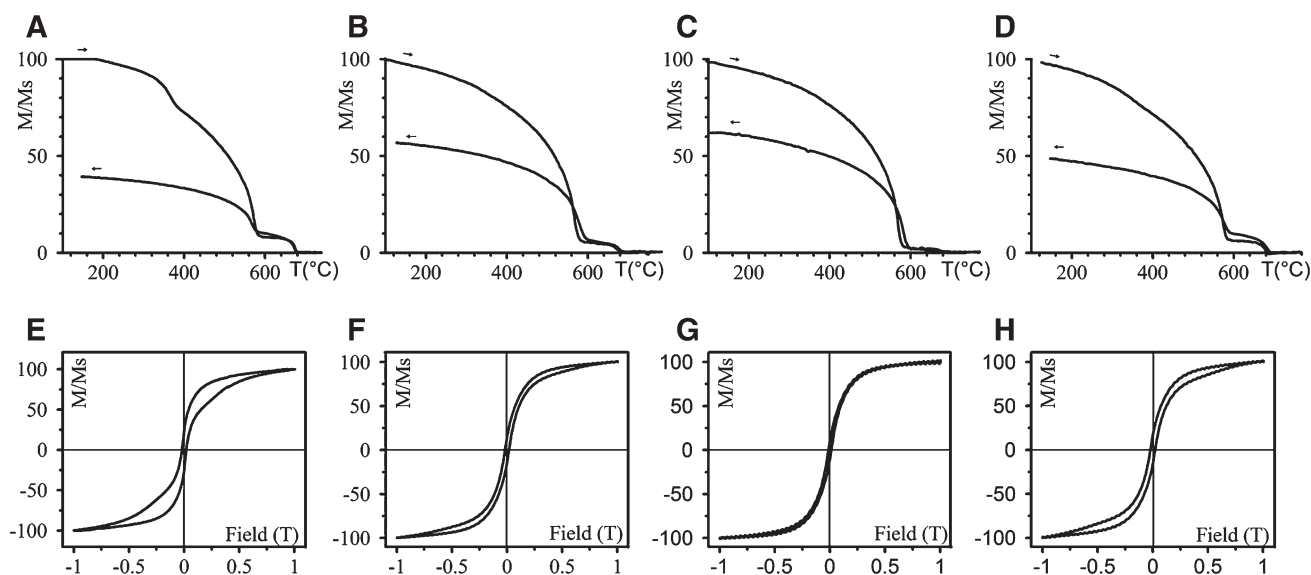


Fig. 7 Thermomagnetic behavior of samples: **a** Brazilian, **b** Indian total, **c** Indian magnetic extraction, **d** Indian rest, after magnetic extraction. Magnetic hysteresis of the samples: **e** Brazilian, **f** Indian

total, **g** Indian magnetic extraction, **h** Indian rest, after magnetic extraction. M/M_s relative magnetization (see discussion in text)

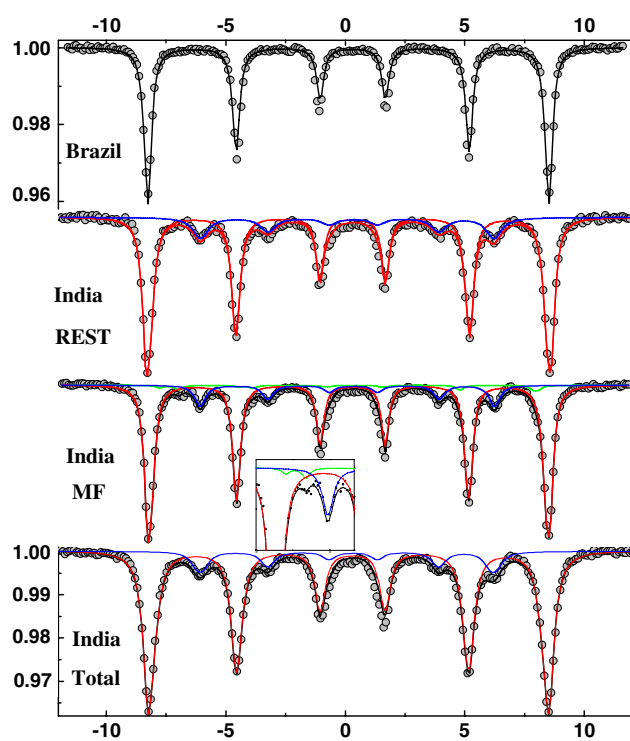


Fig. 8 300-K Mössbauer spectra recorded for the Indian (*TOT* total sample material, *MF* magnetic fraction, *REST* rest after magnetic extraction) and the Brazilian samples

at 617–631 cm^{-1} instead of 613 cm^{-1} , and the position of the magnon band at 1,330–1,340 cm^{-1} (i.e., a shift up to 20 cm^{-1}) are significant. The band at 668–675 cm^{-1} is in the range reported for the strong E_g mode of magnetite

(661–680 cm^{-1} ; de Faria et al. 1997; Shebanova and Lazor 2003b), but a band above 670 cm^{-1} has been attributed by Hanesh (2009) to the ongoing transformation of magnetite reflecting possible maghemite. Furthermore, maghemite exhibits a band at ~1,330–1,360 cm^{-1} , which could contribute here to the apparent shift of the hematite 1,320 cm^{-1} band to a higher wave number (Hanesh, 2009). The band at about 634 cm^{-1} , unusual in hematite, has been reported by Gehring et al. (2009) and interpreted as non-stoichiometric magnetite. The superposition of modes in the bright white parts of same reflectance and apparently homogeneous suggests that the size of some minerals is below the optical detection limit. It is thus concluded that the bands at about 634 and 675 cm^{-1} reflect the presence of maghemite or a non-stoichiometric transformation product of magnetite.

In the darker grayish patches, the spectra are slightly different (red spectrum in Fig. 9b). Besides well-defined peaks at ~226, 296, 414, 505, and 1,328 cm^{-1} corresponding to hematite, shoulders on the flank of, or between defined bands are present, in comparison with the green spectrum from the bright patches (Fig. 9b). In the strong broad band at 669 cm^{-1} , hidden peaks on its flanks are revealed by deconvolution at 565, 612, 730–740 cm^{-1} . Similarly, a hidden peak can be found at ~360 cm^{-1} . These modes indicate thus the presence of relict magnetite (565 and 669 cm^{-1}) and of maghemite (360 and 730–740 cm^{-1} , shown by red arrows in Fig. 9b) or another non-stoichiometric magnetite. The maghemite “diagnostic” bands (Hanesh 2009) are not well defined likely due to a small (less than micrometric) particle size. On this spectrum, the strong band at ~665 cm^{-1} is attributed to both magnetite and maghemite.

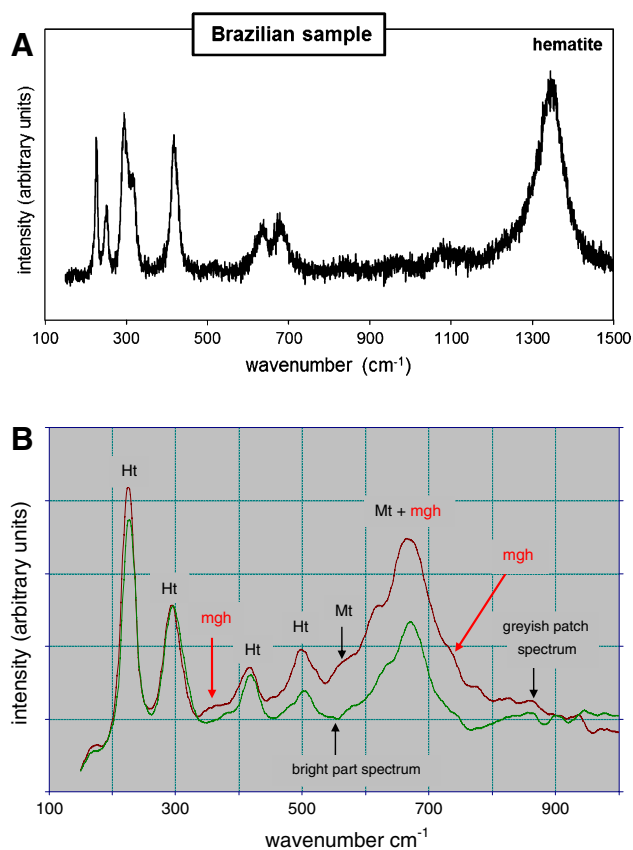


Fig. 9 Raman spectra from the Brazilian sample. **a** Hematite spectrum representative from the bright part. **b** In red, representative partial spectrum from darker grayish patches compared to hematite spectrum (in green). The shoulders (red arrows) are attributed after deconvolution to maghemite (*mgh*) typical bands and magnetite (*Mt*) (black arrow). The other well-defined bands are from hematite (*Ht*), and the broad band at $\sim 665\text{ cm}^{-1}$ is attributed to both magnetite (*Mt*) and maghemite (*mgh*)

408 Indian sample

409 Raman spectra acquired in two different massive Fe-
 410 oxide layers from the Indian sample share the following
 411 characteristics: spectra from the bright white spindle-
 412 shape hematite trellis arranged parallel to [111] direc-
 413 tions (Fig. 2c) show typical bands of hematite at 223–
 414 226, 243–246, 291–298, 408–413, 495–503, 613–624,
 415 and $\sim 1,320\text{ cm}^{-1}$ (Fig. 10a). A band at 660–664 cm^{-1}
 416 may indicate the contribution from magnetite. Additional
 417 unresolved bands hidden in the fluorescence background
 418 between 800 and $1,200\text{ cm}^{-1}$ have also been reported by
 419 Hanesh (2009). The octahedral grains contain rare darker
 420 patches that have two different spectrum types: in type
 421 1, bands at 301, 410, 541, and 666 cm^{-1} (Fig. 10b) are
 422 characteristic of magnetite, and in type 2, bands at 239–
 423 243, 297–299, 383–385, 416–417, 479–480, 548–550,
 424 $\sim 681\text{ cm}^{-1}$ (Fig. 10c) reflect the presence of goethite (de

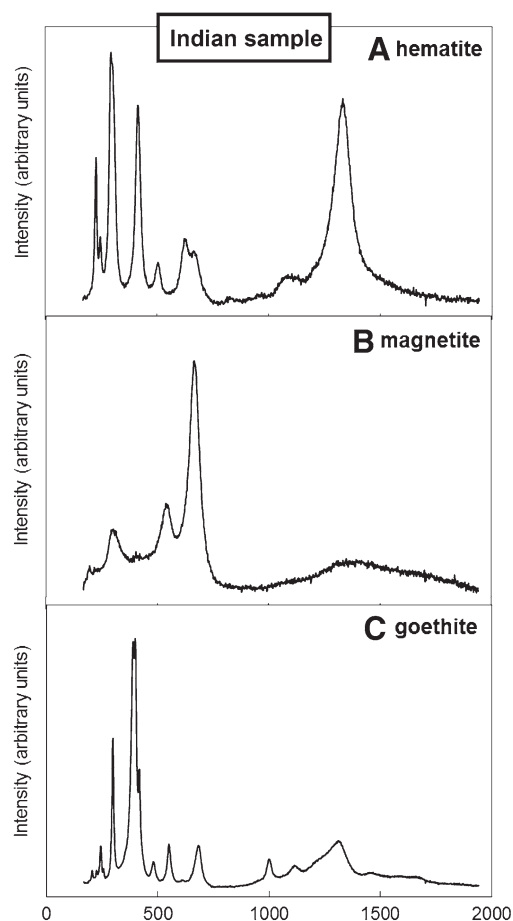


Fig. 10 Representative Raman spectra from the Indian sample. **a** Hematite from the bright hematite trellis, **b** magnetite; and **c** goethite from small rare darker patches (see discussion in text)

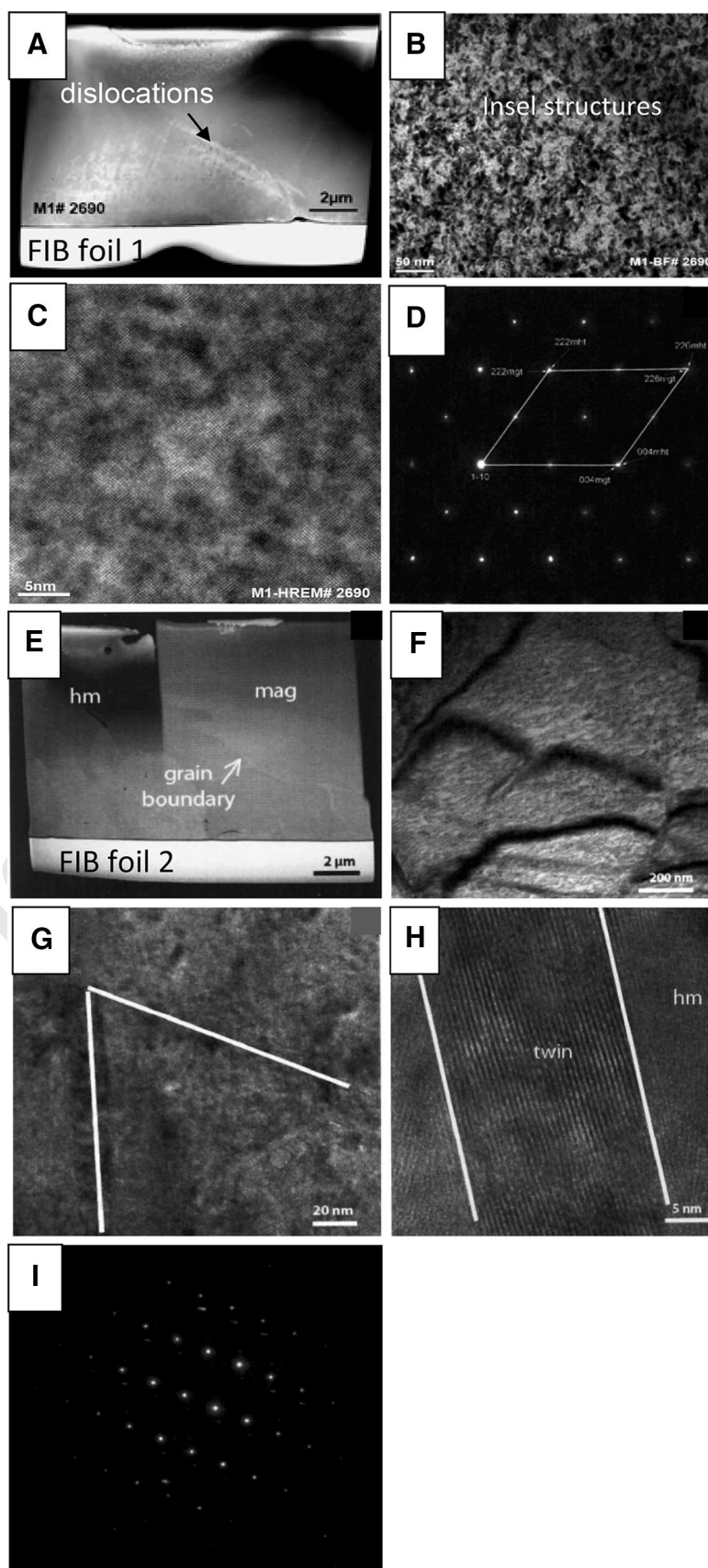
Faria et al. 1997; Hanesh 2009). The additional bands at
 425 $\sim 1,000$, $\sim 1,110$, and $1,300\text{--}1,314\text{ cm}^{-1}$ have also been
 426 reported for synthetic goethite (Hanesh 2009). Mag-
 427 hemite has not been observed.
 428

FIB-TEM

Brazilian sample

431 In the Brazilian sample, two FIB-TEM foils were cut
 432 through magnetite (FIB foil 1; Fig. 11a, d) and through a
 433 hematite–magnetite part (FIB foil 2, Fig. 11e–i). FIB foil 1
 434 represents a single magnetite crystal showing dislocations
 435 in some parts (arrow in Fig. 11a) and a patchy diffraction
 436 contrast (Fig. 11b, c). This mosaic texture of nanometer-
 437 sized Insel structures (black in Fig. 11b) likely indicates
 438 two phases slightly disorientated and/or with different
 439 stoichiometries. The presence of two different phases is
 440 confirmed by the splitting of the reflections in the SAED
 441 pattern (Fig. 11d). The major pattern shows lattice vector

Fig. 11 FIB-TEM investigations on the Brazilian sample. FIB foil 1 in magnetite. **a** Overview of the magnetite crystal with an area rich in dislocations shown by the *arrow* (HAADF image). **b** and **c** Bright field (BF) and complementary HREM images, respectively, showing a patchy diffraction pattern. **d** SAED pattern indexed as magnetite (*mgt*). The splitting of the highest intense peaks reveals the presence of possible maghemite (*mht*). FIB foil 2 through hematite and magnetite. **e** HAADF image of the foil showing the NW–SE crystal boundary between hematite (*hm*) and magnetite (*mag*). **f** BF image of lamellae within the hematite crystal. **g** and **h** BF image showing the directions of two sets of twins and HREM image of a twin set in the hematite matrix, respectively. **i** SAED pattern of hematite with split peaks reflecting a second diffraction pattern that could not be indexed



lengths of 0.4115 and 0.4756 nm with an angle of 54.7° between planes (100) and (111) and lengths of 0.4756 and 0.4737 nm with an angle of 70.53° between planes (-111) and (111), lengths characteristic of magnetite. The second crystal indexed from the split peaks shows the same cubic system, but shorter lengths of the diffraction vector ($111 = 0.4461$ and 0.4756 nm), indicating a shrinking of the crystal lattice and is probably maghemite within magnetite (Fig. 11d).

FIB foil 2 shows Z-contrasted parts of hematite and magnetite (Fig. 11e). The hematite crystals show scattering areas resulting in a patchy contrast as in the magnetite of FIB foil 1 and contain lamellae and twins (Fig. 11f, h). There are at least two sets of simple twins occurring along the (011) planes at angles of 64° and with widths between 7 and 40 nm (Fig. 11g, h). The SAED pattern from the hematite part (Fig. 11i) reveals a second diffraction pattern behind the hematite pattern, as observed in FIB foil 1. For both sets of twins, the second diffraction pattern (not shown) can be indexed as magnetite or maghemite (or another non-stoichiometric magnetite). The SAED image acquired in the magnetite part only shows magnetite reflections.

Indian sample

The FIB foil cut in the Indian sample (Fig. 12a) shows numerous subhedral and interstitial crystals, magnetite and hematite (Fig. 12b), as indexed from the SAED patterns (Fig. 12c, d). As in the Brazilian sample, the magnetite SAED pattern shows split peaks (magnetite and maghemite; Fig. 12c). The d-spacings of the a-axes were 0.421 and 0.414 nm corresponding to magnetite and hematite, respectively. All the magnetite crystals have the same orientation, and their curved interface suggests evidence for grain boundary migration (Fig. 12b). Lamellae, similar to those observed in the Brazilian sample, are present in both magnetite and hematite, but they are much more defined in magnetite (Fig. 12e). The interstitial hematite crystals are characterized by dislocations and a high porosity with fluid inclusions along the dislocation lines (Fig. 12f, g).

Discussion

Cross-cutting results from the different methods

XRD detected hematite as the major compound in both samples. The presence of magnetite was identified by the shoulder of the peak at ~ 2.52 Å in the long-term run of the Brazilian sample and by the clear splitting of this peak

in the magnetic fraction of the Indian sample, while peaks at ~ 2.96 and 1.61 Å in both samples could be attributed to both magnetite and maghemite. Although it is difficult to discriminate between magnetite and maghemite as both have a spinel structure, the presence of maghemite is attested in both samples by the peak at 2.78 Å. Goethite was identified in the Indian sample. The clear differences in the magnetic behavior of hematite and magnetite (easily magnetized and demagnetized) allow identifying a higher content of hematite compared to magnetite in the Brazilian sample than in the Indian sample, inferred from the relative magnetization and the shape of the hysteresis loops. Moreover, maghemite was detected in the Brazilian sample and suspected in the Indian sample. Common 300-K Mössbauer spectroscopy detected hematite in both samples, and magnetite and goethite in the Indian sample, but no maghemite. In-field Mössbauer spectroscopy would help detecting maghemite (Tuček and Zboril 2005). Raman spectroscopy identified hematite in the overall bright parts of the martite grains and magnetite in small darker patches from both samples. Moreover, maghemite or another non-stoichiometric magnetite was identified in the Brazilian sample. Goethite was found in the Indian sample. FIB-TEM analyses detected hematite, magnetite and maghemite in both samples and allowed to determine the phase relation and structures. In the Brazilian sample, maghemite occurs as nanometer-sized blocks arranged in a mosaic texture within magnetite or in twin sets in hematite. In the Indian sample, magnetite and maghemite occurred as subhedral crystals, while hematite forms the interstitial crystals hosting dislocations and fluid inclusions.

Processes of magnetite to hematite transformation

During the replacement of magnetite by hematite, Fe^{2+} ions diffuse through defects of the oxygen framework to surface sites where they are oxidized and either added to the surface or removed by solution (Davis et al. 1968; Lindsley 1976). This leads to vacancies in the spinel structure and the formation of cation-deficient magnetite or of maghemite, which converts to hematite. Alternatively, the transformation of magnetite to hematite may also result from non-redox reactions involving the leaching of Fe^{2+} ions by acidic solutions (Ohmoto 2003; Otake et al. 2007). In both cases, the transformation is accompanied by volume changes. While the redox-driven transformation implies a small volume increase, the non-redox transformation of magnetite to hematite results in a large volume decrease, which would be associated with a large volume of pore spaces created by the leaching of Fe^{2+} ions (Mücke and Cabral 2005).



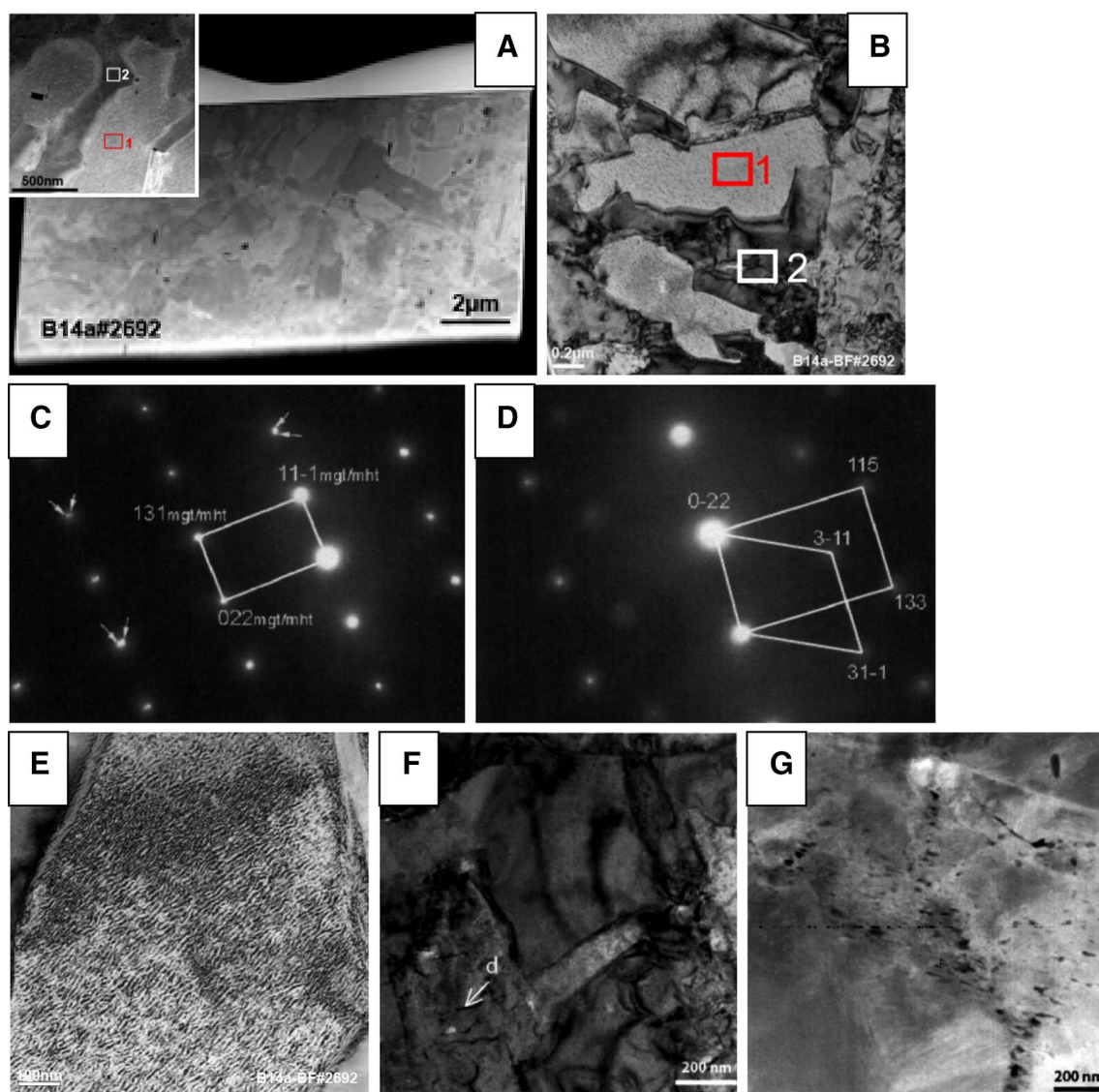


Fig. 12 FIB-TEM investigations on the Indian sample. **a.** Overview of the FIB foil (HAADF image) with a zoomed *inset*. It shows the interface between numerous subhedral *bright* (1) and *interstitial darker* (2) crystals. **b.** BF image of the curved interface between magnetite (1) and hematite (2). **c.** SAED pattern of the subhedral mag-

netite, which shows the splitting of the diffraction peaks, indexed as magnetite (*mgf*) and maghemite (*mht*). **d.** SAED pattern of the interstitial hematite. **e.** BF image of the lamellae in magnetite. **f.** High density of dislocations *d* (BF image). **g.** High porosity and fluid inclusions in the hematite interstitial crystals (HAADF image)

538 The Indian martite shows a trellis structure similar to
 539 the mesh-textured martite reported in different BIFs from
 540 Western Australia (e.g., Morris 1980, 1985; Angerer et al.
 541 2012). The trellis structure may be weathering-related by
 542 oxidation of magnetite (Angerer et al. 2012), as well as
 543 hydration of maghemite (Morris 1980, 1985) or non-stoi-
 544 chiometric magnetite. The latter process leads to the for-
 545 mation of goethite, which is subsequently leached. How-
 546 ever, trellis textures may be also caused through deuteric
 547 high-temperature oxidation followed by hydrothermal
 548 alteration (Alva-Valdivia and Urrutia-Fucugauchi 1998).

In the Indian martite, the lamellae observed in the magnetite grains may reflect magnetite–maghemite intergrowths (Fig. 12e). The presence of magnetite and maghemite in the subhedral crystals and interstitial crystals of hematite may suggest an exsolution process along parting planes leaving behind subhedral magnetite crystals with the same crystallographic orientation. The curved interfaces between magnetite–maghemite and hematite indicate typical grain boundary migrations and dynamic crystallization of hematite, being related to a deformation event. Furthermore, the observed porosity and the fluid inclusions in the

549
 550
 551
 552
 553
 554
 555
 556
 557
 558
 559

560 hematite interstitial crystals point to the presence of a fluid
561 along the hematite interface. This interpretation is consist-
562 ent with the geological environment: the Indian martite-
563 hosting BIF was affected by greenschist facies metamor-
564 phism related to the emplacement of the post-kinematic
565 Chitradurga granite (2.60 ± 0.02 Ga) and to gold miner-
566 alization during compressional tectonics at 2.52 Ga (Tay-
567 lor et al. 1984; Kolb et al. 2004; Jayananda et al. 2006;
568 Sarma et al. 2011). These oxidizing hydrothermal fluids
569 dissolved carbonate minerals and precipitated hematite-
570 magnetite spherules in cavities (Orberger et al. 2012). The
571 transformation from magnetite into hematite and the trellis
572 formation are thus attributed to this hydrothermal event, as
573 proposed by Beukes et al. (2008) for the origin of porous
574 martite from the Archean BIFs at Noamundi, NE India.
575 Later weathering is, however, indicated by the presence
576 of goethite and the porous mesh texture resulting from its
577 partial dissolution.

578 The Brazilian martite has no trellis, but shows irregu-
579 lar patches of magnetite within hematite, and neofomed
580 euhedral tabular hematite crystals (Fig. 1b). Davis et al.
581 (1968) attributed the epitaxial magnetite replacement by
582 hematite to a relative volume decrease of 7.8 vol% during
583 the first step of the transformation of magnetite into magh-
584 emite. According to Barbosa and Lagoeiro (2010), the ori-
585 ented growth of tabular hematite crystals is controlled by
586 the octahedral planes of old magnetite grains, and, when
587 dislocations are present, may be influenced by these crys-
588 tal defects. For these authors, the direct transformation
589 from magnetite into hematite occurs without the interme-
590 diate step of maghemite. However, the here studied martite
591 clearly shows features indicating that the transformation
592 comprises a maghemite step: (1) in hematite, the presence
593 of lamellae and twins (Fig. 11h). The lamellae result from
594 a structural change without chemical change, i.e., they still
595 have the hematite chemistry, but a maghemite structure.
596 The alignment along (111) of the structural defects created
597 by the formation of maghemite is reflected by the observed
598 lattice twins, the remnants of which are visible in the
599 lamellae; (2) in magnetite, non-stoichiometric zones (Insel
600 structures) and nano-scale dislocations, pointing to defor-
601 mation (Fig. 11a, b). It is suggested that this deformation
602 initiated the transformation from magnetite via magh-
603 emite into hematite along crystal planes. This scenario is
604 in agreement with the geological history of the underly-
605 ing phyllites and hydrothermal veins, which experienced
606 later deformation (Cabral et al. 2011, 2012). The above-
607 outlined arguments favor thus a fluid-deformation-induced
608 magnetite-hematite transformation via a maghemite step
609 prior to lateritization.

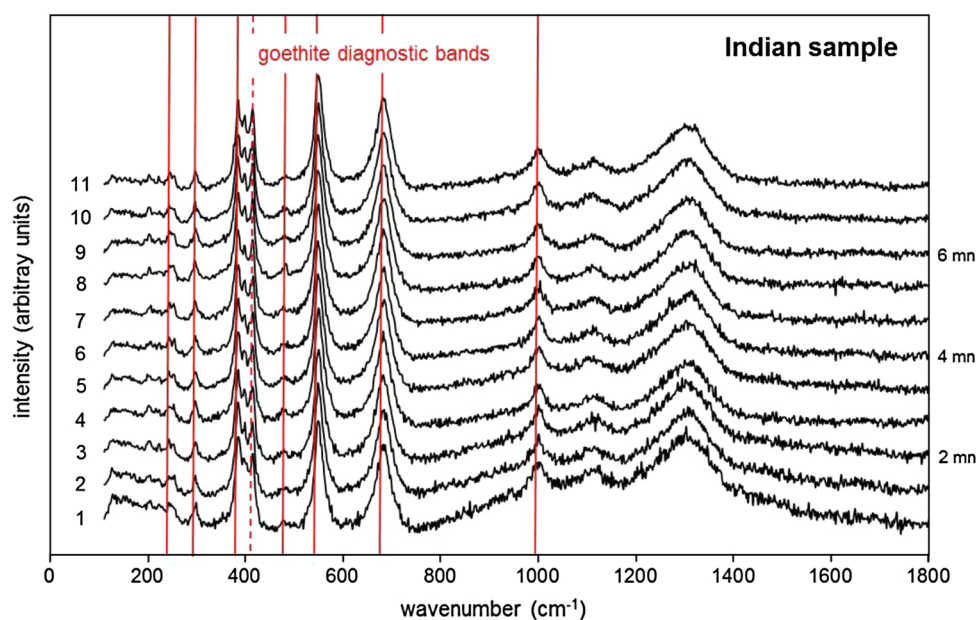
Conclusion

611 The analytical methods used during this study give comple-
612 mentary information, as different physical properties
613 are analyzed at different scales. In both samples, hema-
614 tite was detected as the major, and magnetite as the minor
615 component, as these minerals have clear different mag-
616 netic behavior. Raman spectroscopy detects maghemite
617 or a non-stoichiometric magnetite. XRD spectra show
618 a small peak at 2.78 \AA indicative for maghemite. FIB-
619 TEM shows clear deformation structure (grains bound-
620 ary migration, dislocations and twinning). Although
621 deformation features differ in the two studied martites, in
622 agreement with the geological environment, deformation-
623 induced oxidizing fluids are proposed for the transfor-
624 mation of magnetite into hematite via a maghemite step
625 for both samples. This study shows that martite found in
626 supergene environment may result from earlier hypogene
627 processes.

628 **Acknowledgments** This project was funded by the national PNP
629 Planétologie, PRES UNIVERSUD Planétologie and the UMR IDES
630 8148 (CNRS-UPS) and COFECUB-CAPES (UPS, Orsay France-
631 UFMG, Belo Horizonte, Brazil). It was part of the ESF project
632 “Early Habitats of Early life”. The authors thank Rémy Pichon, Luce
633 Delabesse, Valérie Godard and Olivier Dufour (UMR IDES), Gilles
634 Montagnac (ENS-Lyon, Lyon) and Anja Schreiber (GFZ-Potsdam)
635 for technical help. The authors thank M. Rieder for handling the ma-
636 nuscript, A. Cabral, H. Siemes and T. Angerer for comments and sug-
637 gestions to fundamentally improve the manuscript.

Appendix

638
639 Raman spectra of goethite in the Indian sample. The
640 spectra were acquired under the conditions reported in
641 the text and at the same spot every 40 s. Red lines cor-
642 respond to the position of active modes for goethite (de
643 Faria et al. 1997; Hanesh 2009). A band at $\sim 418 \text{ cm}^{-1}$
644 (dashed red line) on the wing of the largest peak at
645 385 cm^{-1} has also been reported by Hanesh (2009).
646 According to these authors, the broad bands above
647 $1,000 \text{ cm}^{-1}$ are not “diagnostic” for goethite and may
648 record some contaminant species. Apart from a decrease
649 in the background fluorescence between 1,000 and
650 $1,400 \text{ cm}^{-1}$ with increasing laser exposition time, there
651 is no significant variation in the observed spectral modes,
652 either in position or in intensity, for a total time of irra-
653 diation up to 8 min. Moreover, there is no appearance of
654 new bands, which would indicate a possible transforma-
655 tion of goethite under the laser beam (in maghemite or
656 hematite; Hanesh 2009).
657



658 References

- 659 Alva-Valdivia LM, Urrutia-Fucugauchi J (1998) Rock magnetic prop-
660 erties and ore microscopy of the iron ore deposit of Las Truchas,
661 Michoacan, Mexico. *J Appl Geophys* 38:277–299
- 662 Angerer T, Hagemann SG, Danyushevsky V (2012) Geochemical evolu-
663 tion of the Banded iron formation-hosted high-grade iron ore
664 system in the Koolyanobbing Greenstone Belt, Western Australia.
665 *Econ Geol* 107:599–644
- 666 Bachmann HG (1954) *Über Martiterte von Talberg (Viermland)*
667 *Schweden. Neues Jahrb Mineral* 6:131–136
- 668 Banerji PK (1984) On some geochemical features of the vanadiferous
669 magnetite deposits of Kumhardubi and Betjharan, Mayurbhanj
670 district, Orissa, India. *Chem Geol* 43:257–269
- 671 Barbosa PF, Lagoeiro L (2010) Crystallographic texture of the mag-
672 netite-hematite transformation: evidence for topotactic relation-
673 ships in natural samples from Quadrilátero Ferrífero, Brazil. *Am*
674 *Mineral* 95:118–125
- 675 Beukes NJ, Mukhopadhyay J, Gutzmer J (2008) Genesis of high-
676 grade iron ores of the Archean iron ore group around Noamundi,
677 India. *Econ Geol* 103:365–386
- 678 Brown DA, Sherrif B, Sawick JA (1997) Microbial transformation of
679 magnetite to hematite. *Geochim Cosmochim Acta* 61:3341–3348
- 680 Cabral AR, Lehman B, Tupinamba M, Wiedenbeck M, Brauns M
681 (2011) Geology, mineral chemistry and tourmaline B isotopes
682 of the Córrego Bom Sucesso area, southern. Serra do Espinhaço,
683 Minas Gerais, Brazil: implications for Au–Pd–Pt exploration in
684 quartzitic terrain. *J Geochem Explor* 110:260–277
- 685 Cabral AR, Wiedenbeck M, Koglin N, Lehmann B, de Abreu FR
686 (2012) Boron-isotopic constraints on the petrogenesis of hemat-
687 itic phyllite in the southern Serra do Espinhaço, Minas Gerais,
688 Brazil. *Lithos* 140–141:224–233
- 689 Colombo U, Cazzarini F, Lanzavecchia G, Sironi E (1965) Magnetite
690 oxidation: a proposed mechanism. *Science* 147:1033
- 691 Davis BL, Rapp G, Walawender MJ (1968) Fabric and structural char-
692 acteristics of the martitisation process. *Am J Sci* 266:482–496
- 693 Day R, Fuller MD, Schmidt VA (1977) Magnetic hysteresis properties
694 of synthetic titanomagnetites. *Phys Earth Planet Inter* 13:260–266
- 695 De Boer CB, Dekkers MJ (2001) Unusual thermomagnetic behaviour
696 of haematites: neoformation of a highly magnetic spinel phase on
697 heating in air. *Geophys J Int* 144:481–494
- de Faria DLA, Venancio-Silva S, de Oliveira MT (1997) Raman
698 microspectroscopy of some iron oxides and oxyhydroxides. *J*
699 *Raman Spectrosc* 28:873–878
- El Mendili Y, Bardeau JF, Randrianantoandro N, Gourbil A, Greneche
700 JM, Mercier AM, Grasset F (2010) New evidence of in situ laser
701 irradiation effects on γ -Fe₂O₃ nanoparticles: a Raman spectro-
702 scopic study. *J Raman Spectrosc* 42:239–242
- Gehring AU, Fischer H, Louvel M, Kunze K, Weidler PG (2009) High
703 temperature stability of natural maghemite: a magnetite and spec-
704 troscopic study. *Geophys J Int* 179:1361–1371
- 705 Gruner JW (1922) Organic matter and the origin of the Biwabik iron-
706 bearing formation of the Mesabi range. *Econ Geol* 17:407–460
- 707 Gruner JW (1926) Magnetite–martite–hematite. *Econ Geol* 21:
708 375–393
- 709 Gruner JW (1929) Structural reasons for oriented intergrowths in
710 some minerals. *J Mineral Soc Am* 14:227–231
- 711 Hanesh M (2009) Raman spectroscopy of iron oxides and (oxy)
712 hydroxides at low laser power and possible implications in envi-
713 ronmental magnetic studies. *Geophys J Int* 177:941–948
- 714 Jayananda M, Chardon D, Peucat J-J, Capdevila R (2006) 2.61 Ga
715 potassic granites and crustal reworking in the western Dharwar
716 craton, Southern India: tectonic, geochronological and geochemi-
717 cal constraints. *Precambrian Res* 150:1–26
- 718 Joint Committee on Powder Diffraction Standard (1974) Selected
719 powder diffraction data for minerals. Joint Committee on Powder
720 Diffraction Standards, Pennsylvania
- 721 Kolb JH, Rogers A, Sinderen S, Vennemann T, Böttcher ME, Meyer
722 FM (2004) The role of a transcrustal shear zone in orogenic gold
723 mineralization at the Ajjanahalli mine, Dharwar craton, South
724 India. *Econ Geol* 99:743–759
- 725 Kullerud G, Donnay G, Donnay JDH (1969) Omission solid solu-
726 tion in magnetite: kenotetrahedral magnetite. *Z Kristallogr Bd*
727 128:1–17
- 728 Kumar B, Das Sharma S (1998) Carbon isotope systematics of graph-
729 ites from Dharwar craton, Southern India: implications to their
730 source and post-depositional alterations. *Curr Sci* 75:396–397
- 731 Lagoeiro LE (1998) Transformation of magnetite to hematite and its
732 influence on the dissolution of iron-oxide minerals. *J Metamorph*
733 *Geol* 16:415–423
- 734 Lepp H (1957) Stages in the oxidation of magnetite. *Am Mineral*
735 42:679–681

- 739 Lindsley DH (1976) Experimental studies of oxide minerals. In:
740 Rumble D III (ed) Reviews of mineralogy, oxide minerals, vol
741 32, 2nd edn. BookCrafters, Chelsea, pp L61–L88
- 742 Morris RC (1980) A textural and mineralogical study of the relation-
743 ship of iron ore to banded iron ore formation in the Hamersley
744 iron province of Western Australia. *Econ Geol* 75:184–209
- 745 Morris RC (1985) Genesis of iron ore in banded iron formation by
746 supergene and supergene-metamorphic processes—a conceptual
747 model. In: Wolf KH (ed) Handbook of strata-bound and strati-
748 form ore deposits, vol 13. Elsevier, Amsterdam, pp 73–235
- 749 Mücke A, Cabral AR (2005) Redox and non-redox reactions of mag-
750 netite and hematite. *Chem Erde* 65:271–278
- 751 Ohmoto H (2003) Non-redox transformations of magnetite–hematite
752 in hydrothermal systems. *Econ Geol* 98:157–161
- 753 Orberger B, Wagner C, Wirth R, Quirico E, Gallien JP, Derré C, Mon-
754 tagnac G, Noret A, Jayananda M, Massault M, Rouchon V (2012)
755 Origin of iron-oxide spherules in the banded iron formation of
756 the Bababudan Group, Dharwar Craton, Southern India. *J Asian
757 Earth Sci* 52:31–42
- 758 Otake T, Wesolowski DJ, Anovt LM, Allard LF, Ohmoto H (2007)
759 Experimental evidence for non-redox transformations between
760 magnetite and hematite under H₂-rich hydrothermal conditions.
761 *Earth Planet Sci Lett* 257:60–70
- 762 Roberts AP, Cui Y, Verosub KL (1995) Wasp-waisted hysteresis
763 loops: mineral magnetic characteristics and discrimination
764 of components in mixed magnetic systems. *J Geophys Res*
765 100(B9):17909–17924
- 766 Sarma SD, Fletcher IR, Rasmussen B, McNaughton NJ, Mohan MR,
767 Groves DI (2011) Archean gold mineralization synchronous with
768 late cratonization of the Western Dharwar Craton, India: 2.52 Ga
769 U–Pb ages of hydrothermal monazite and xenotime in gold
770 deposits. *Miner Depos* 46:273–288
- 771 Shebanova ON, Lazor P (2003a) Raman study of magnetite (Fe₃O₄):
772 laser-induced thermal effects and oxidation. *J Raman Spectrosc*
773 34:845–852
- 774 Shebanova ON, Lazor P (2003b) Raman spectroscopic study of mag-
775 netite (FeFe₂O₄): a new assignment for vibrational spectrum. *J
776 Solid State Chem* 174:424–430
- Srinivasan R, Ojakangas RW (1986) Sedimentology of quartz-pebble 777
conglomerates and quartzites of the Archaean Bababudan Group, 778
Dharwar Craton, South India: evidence for early crustal stability. 779
J Geol Soc India 94:199–214 780
- Swanson-Hysell NL, Feinberg JM, Berquô TS, Maloof AC (2011) 781
Self-reversed magnetization held by martite in basalt flows from 782
the 1.1 billion-year-old Keweenaw-rift, Canada. *Earth Planet* 783
Sci Lett 325:171–184 784
- Tarling DH (1983) Paleomagnetism, principles and applications in 785
geology, geophysics and archaeology. Chapman and Hall, New 786
York 787
- Tauxe L, Mullender TAT, Pick T (1996) Potbellies, wasp-waisted, 788
and superparamagnetism in magnetic hysteresis. *J Geophys Res* 789
101(B1):571–583 790
- Taylor PN, Chadwick B, Moorbath S, Ramakrishnan M, Viswanatha 791
MN (1984) Petrography, chemistry and isotopic ages of penin- 792
sular gneisses, Dharwar, acid volcanics and Chitradurga granite 793
with special reference to Archaean evolution of Karnataka craton, 794
Southern India. *Precambrian Res* 23(3–4):349–375 795
- Thompson R, Oldfield M (1986) Environmental magnetism. Allen 796
and Unwin, London 797
- Tuček J, Zboril R (2005) Zero-field and in-field Mössbauer spec- 798
troscopy as a tool for structural and magnetic characteriza- 799
tion of maghemite (γ-Fe₂O₃) nanoparticles. *Czechoslov J Phys* 800
55:893–911 801
- Wasilewski P (1973) Magnetic hysteresis in natural materials. *Earth* 802
Planet Sci Lett 20:67–72 803
- Weber H-P, Hafner SS (1971) Vacancy distribution in nonstoichiomet- 804
ric magnetites. *Z Kristallogr New Cryst Struct* 133:327–340 805
- Wirth R (2004) Focused Ion Beam (FIB): a novel technology for 806
advanced application of micro-and nanoanalysis in geosciences 807
and applied mineralogy. *Eur J Mineral* 16:863–876 808
- Wirth R (2009) Focused ion beam (FIB) combined with SEM and 809
TEM: advanced analytical tools for studies of chemical compo- 810
sition, microstructure and crystal structure in geomaterials on a 811
nanometer scale. *Chem Geol* 261:217–229 812
813

